Journal of Power Sources 196 (2011) 4762–4768

Contents lists available at ScienceDirect

Journal of Power Sources

journal homepage: www.elsevier.com/locate/jpowsour

Nanostructured Si/Sn–Ni/C composite as negative electrode for Li-ion batteries

Z. Edfouf[a], F. Cuevas[a,*], M. Latroche[a], C. Georges[a], C. Jordy[b], T. Hézèque[b], G. Caillon[b], J.C. Jumas[c], M.T. Sougrati[c]

[a] CMTR – ICMPE, UMR7182, CNRS, 2-8 rue Henri Dunant, Thiais 94320 Cedex, France
[b] SAFT Batteries, 113 Bd, Alfred Daney, 33074 Bordeaux Cedex, France
[c] ICGM, UMR 5253, CNRS. Université Montpellier 2-CC 1700 Place Eugène Bataillon, 34095 Montpellier Cedex 5, France

ARTICLE INFO

Article history:
Received 5 November 2010
Received in revised form 3 January 2011
Accepted 16 January 2011
Available online 26 January 2011

Keywords:
Lithium ion battery
Anode material
Ball milling
Si
Sn–Ni intermetallics

ABSTRACT

A nanostructured composite with overall atomic composition $Ni_{0.14}Sn_{0.17}Si_{0.32}Al_{0.037}C_{0.346}$ has been prepared combining powder metallurgy and mechanical milling techniques for being used as anode material in Li-ion battery. Chemical and structural properties of the nanocomposite have been determined by X-ray diffraction (XRD), ^{119}Sn Transmission Mössbauer Spectroscopy (TMS), scanning electron microscopy (SEM) and transmission electron microscopy (TEM). The composite consists of Si particles with typical size ~150 nm embedded in a poorly crystallized and complex multielemental matrix. The matrix is composed mostly by $Ni_{3.4}Sn_4$, and disordered carbon. Electrochemical evaluation shows a high reversible capacity of 920 mAh g^{-1}, with reasonable reversible capacity retention (~0.1% loss/cycle) over 280 cycles.

1. Introduction

Research on Li-ion batteries knows a significant growth due to their superior performances as compared to other rechargeable batteries. The majority of the marketed lithium ion batteries use carbon graphite as negative electrode which provides a long cycle life thanks to its stable morphology avoiding dendritic growth and minimizing safety concerns. Its theoretical specific capacity is 372 mAh g^{-1} for LiC_6 [1], though in reality this capacity remains limited to 350 mAh g^{-1} due to the loss of capacity during formation of the surface electrolyte interface (SEI) [2,3], and incomplete lithium extraction from graphite layers. Presently a lot of materials are studied as alternatives for carbonaceous materials in order to enhance the energy densities of the negative electrode. Indeed a special interest is devoted to pure p-type elements that form lithiated compounds [4]. For instance Sn and Si can form $Li_{4.4}Sn$ and $Li_{4.4}Si$ compounds to store 994 and 4200 mAh g^{-1} in equivalent electrochemical units, respectively, leading to much higher capacities than that of carbon graphite [5]. However, electrodes made up of pure elements are generally considered inappropriate because of huge capacity fading during the first electrochemical cycles. The large volume expansion that accompanies Li insertion and extraction during cycling results in electrode pulverization and loss of electrical contact [6,7].

To improve mechanical stability, embedding capacitive elements into a non active matrix that could accommodate volume changes seems to be a good solution. This concept can be implemented by using binary intermetallic compounds consisting of an element that reacts with lithium and another one that is inactive. Some examples are Ni_3Sn_4 [8–11], Cu_6Sn_5 [12], $FeSn_2$ [13], $NiSi_2$ [14] and FeSi [15]. On electrochemical lithiation, the volume expansion related to the formation of Si–Li (or Sn–Li) compounds is buffered by the inactive transition metal which prevents the coalescence of the active material during cycling. Moreover, the presence of metallic phases will improve the electric conductivity within the electrode. Furthermore, if the active material is downsized at the nanoscale, this shortens the diffusion length for lithium insertion and increases the surface area of the active material leading to lower charge transfer resistance of the electrodes [16,17]. Therefore, nanostructured composites that contain intermetallic compounds are good candidates to be used as acceptable cycle life anode materials.

In this work, we study the electrochemical properties of a new nanostructured composite material with overall atomic composition $Ni_{0.14}Sn_{0.17}Si_{0.32}Al_{0.037}C_{0.346}$. The composite consists of sub-micrometric Si particles embedded in a nanostructured and complex matrix mainly formed by $Ni_{3.4}Sn_4$ intermetallic compound and disordered carbon. This matrix also contains minor quantities of Al, Si and Sn. The addition of Al was chosen following its beneficial effect on the cycle-life of Si–Sn–Al amorphous elec-

* Corresponding author. Tel.: +33 1 49781225; fax: +33 1 49781203.
E-mail address: fermin.cuevas@icmpe.cnrs.fr (F. Cuevas).

0378-7753/$ – see front matter © 2011 Elsevier B.V. All rights reserved.
doi:10.1016/j.jpowsour.2011.01.046

trodes [18]. Si and Sn are the most capacitive elements whereas Ni and C are expected to accommodate the volume changes and to insure good electronic and ionic conductivities of the electrode material.

2. Experimental

The nanostructured composite $Ni_{0.14}Sn_{0.17}Si_{0.32}Al_{0.037}C_{0.346}$ was made by a two-step procedure. Firstly a tin based intermetallic precursor $Ni_{3.4}Sn_4$ was synthesized by powder metallurgy followed by mechanical milling of the precursor together with Si, Al and C elements. To synthesize $Ni_{3.4}Sn_4$, elemental nickel (99.9%, <45 μm, Cerac) and tin (99.9%, <45 μm, Alfa-Aesar) powders were weighted in 3.4:4 stoichiometric ratio and well mixed under argon atmosphere. The mixed powder was mechanically pressed to metallic pellets and was sintered under argon atmosphere in a silica tube at 700 °C for 7 days. The pellets were then mechanically pulverized down to 100 μm size. Next, powders of silicon (99.9%, <1 μm), aluminum (99%, ≤75 μm, Aldrich), graphite and $Ni_{3.4}Sn_4$ precursor were weighed according to the nominal composite composition and mechanically milled in a Fritsch P7 planetary mill. Ball milling was performed under argon atmosphere for 1 h, 5 h, 10 h and 20 h in a 35 ml volume jar with 7 mm diameter balls. The ball to powder weight ratio is 5:1. Both jar and balls are made of hardened steel. Vial rotation speed of the mill is 600 rpm. Few milligrams were taken out for X-ray diffraction (XRD) analysis after each step of milling.

The chemical composition of the intermetallic precursor was determined by Electron Probe Micro Analysis (EPMA) in a Cameca SX-100 device. Its crystal structure and that of milled composites were analyzed by XRD with a Bruker AXS D8 θ-θ diffractometer equipped with a rear graphite monochromator using CuK_α radiation. Diffraction patterns were analyzed by the Rietveld method using the FullProf software [19].

The morphology of 20 h-milled composite was studied by scanning electron microscopy (SEM) using a SEM-FEG LEO 1530 device. Its microstructural and chemical properties were analyzed using transmission electron microscopy (TEM) in a Tecnai F20 device. Images were taken in both bright and dark fields. Elemental mapping analysis was carried out by energy-dispersive-X-ray (EDX) analysis in STEM mode. The sample was prepared by mixing the composite with Cu powder, followed by cold-rolling and thinning with argon ions in a GATAN precision ion polishing system. The presence of Sn-containing phases was also determined by ^{119}Sn Transmission Mössbauer Spectroscopy (TMS). TMS measurements were carried out at room temperature with a EG&G constant acceleration spectrometer using a $Ca^{119m}SnO_3$ γ-ray source. The isomer shifts are given relative to $BaSnO_3$ which is used as the standard reference. All spectra were refined with Lorentzian profiles, by the least-squares method, and the quality of the fit was controlled by the usual χ^2 test.

Electrochemical measurements were carried out by galvanostatic cycling in a half coin type cell. Working electrode material was prepared by mixing 40 wt.% of the 20 h-milled composite sieved under 36 μm, 30 wt.% of binder in a fine powder of carboxymethyl-cellulose (CMC) and 30 wt.% of carbon black. Metallic lithium was used as counter negative electrode separated by a 1 M solution electrolyte of $LiPF_6$ dissolved in ethylene carbonate (EC)/ propylene carbonate (PC)/ dimethyl carbonate (DMC) (1:1:3, v/v/v), supported by a microporous polyolefin Celgard membrane and a nonwoven polyolefin separator. The battery was assembled in an argon filled glove box. The experiments were performed using a Biologic potentiostat instrument at a rate of *C*/10. Reference cycles at a rate of *C*/50 were done at the three first cycles and after each 20 cycles. The voltage window was between 70 mV and 2 V. Only reference cycles are reported in this paper.

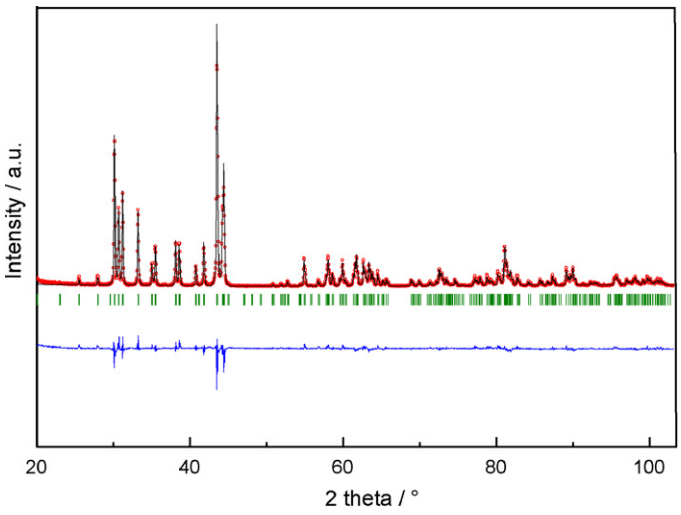

Fig. 1. XRD pattern and Rietveld analysis of $Ni_{3.4}Sn_4$ precursor prepared by powder metallurgy. Observed (dots), calculated (line) and difference (below) curves are shown. The vertical marks show the Bragg positions for the $Ni_{3.4}Sn_4$ phase.

3. Results and discussion

3.1. Structural characterization

The structure and composition of the intermetallic $Ni_{3.4}Sn_4$ precursor have been analyzed by XRD and EPMA techniques, respectively. Fig. 1 shows the Rietveld analysis of the XRD pattern. The sample is single-phase. All diffraction peaks can be indexed in the monoclinic symmetry with *C*2/*m* space group and unit cell parameters $a = 12.435 \pm 0.003$ Å, $b = 4.0780 \pm 0.003$ Å, $c = 5.2093 \pm 0.003$ Å and $\beta = 103.67 \pm 0.02°$. This result concurs with a previous report of Furuseth et al. on $Ni_{3.4}Sn_4$ compound [20]. In this structure Sn atoms fully occupy two different sites with Wyckoff positions $4i_1$ (0.43 ± 0.01, 0, 0.70 ± 0.01) and $4i_2$ (0.18 ± 0.01, 0, 0.82 ± 0.01) whereas Ni atoms fully occupy 2a (0, 0, 0) and $4i_3$ (0.21 ± 0.01, 0, 0.34 ± 0.01) sites and partially occupy 2c (0, 0, ½) sites. Such partial occupancy allows for Ni overstoichiometry in the compound as compared to Ni_3Sn_4. The refined occupancy of 2*c* sites by Ni atoms is equal to 0.4 ± 0.1, which corresponds to a refined composition $Ni_{3.4\pm0.1}Sn_4$. The EPMA analysis of this compound yields as atomic composition $Ni_{3.54\pm0.10}Sn_{4.00\pm0.1}$ in rather good agreement with the Rietveld analysis.

Fig. 2 shows the evolution of the XRD patterns of the $Ni_{0.14}Sn_{0.17}Si_{0.32}Al_{0.037}C_{0.346}$ composite with milling time. After one hour of milling, diffraction lines from $Ni_{3.4}Sn_4$ and Si phases are clearly identified, but those of Al and graphite are not detected anymore. The absence of Al lines is mainly related to its low content (3.7 at.%), though solubility of this metal in other phases cannot be ruled out. As for the disappearance of graphite lines, it is attributed to loss of crystallinity on milling. With increasing milling time significant peak-broadening of $Ni_{3.4}Sn_4$ lines occurs. At 5 h of milling an additional peak attributed to Sn-phase appears but it becomes invisible with further milling due to severe peak broadening of $Ni_{3.4}Sn_4$ phase. Tin phase appearing at 5 h milling is expected to be a product of a reaction between Si and $Ni_{3.4}Sn_4$ phases. This assumption is based on complementary experiments (not shown in this paper) for which milling the same reactants without carbon leads to the full consumption of the $Ni_{3.4}Sn_4$ phase into Sn and Ni–Si by-products. In this work, carbon slows down the previous reaction. Finally, after 20 h milling, the XRD pattern exhibits

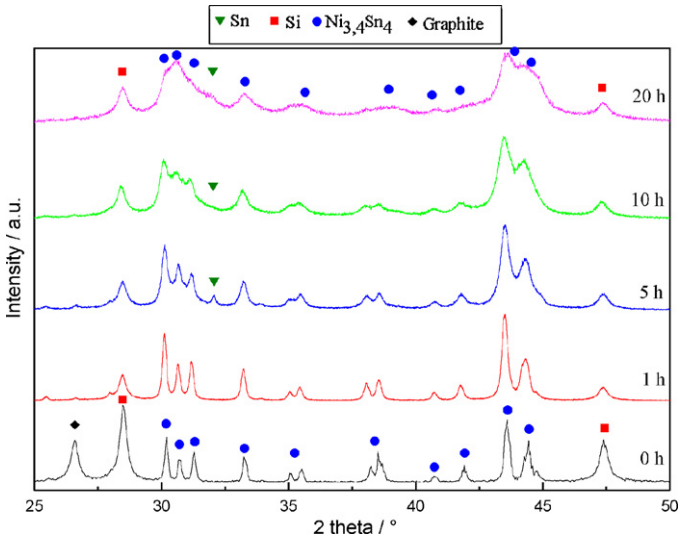

Fig. 2. Evolution of XRD patterns of $Ni_{0.14}Sn_{0.17}Si_{0.32}Al_{0.037}C_{0.346}$ composite with milling time from 0 to 20 h.

strong peak-broadening which reflects the nanostructured state of the composite.

Fig. 3 shows the Rietveld analysis of the 20 h-milled composite. The XRD pattern was refined with three phases: $Ni_{3.4}Sn_4$ (monoclinic C2/*m*), β-Sn (tetragonal $I4_1/amd$) and Si (cubic $Fd\bar{3}m$). In addition, two large diffraction bumps centered at ~38° and 72° were detected showing partial sample amorphisation. This amorphous phase maybe related to Ni–Si by-products. Table 1 gathers the structural and microstructural data obtained from the Rietveld analysis of the 20 h-milled composite, together with the pure Sn and Si elements used in this study. Unit cell parameters of the three detected phases are very close to those of the intermetallic precursor and the pure elements. The phase content of the composite remains essentially constant on milling since $Ni_{3.4}Sn_4$ and Si phases are preserved, only a small quantity of Sn is produced after 20 h of milling. As for the microstructural parameters, ball milling strongly reduces the crystal size of $Ni_{3.4}Sn_4$ to the low nano-scale range (6 nm) and, in a lesser extent, that of Si (14 nm). The crystal size of the Sn phase by-product is also nanocrystalline (9 nm).

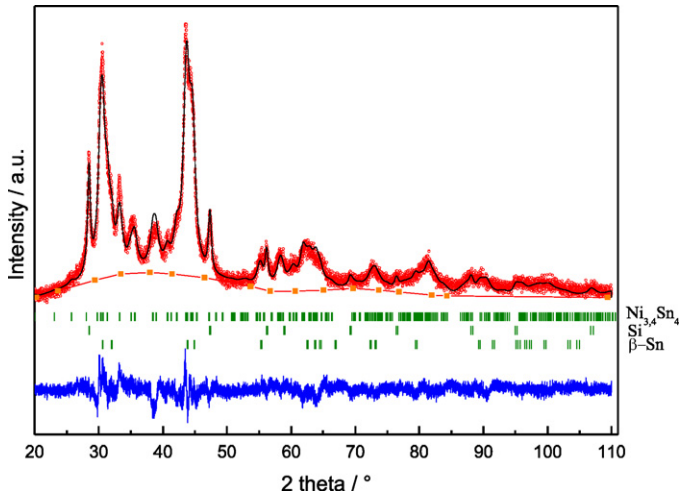

Fig. 3. XRD pattern and Rietveld analysis of 20 h-milled $Ni_{0.14}Sn_{0.17}Si_{0.32}Al_{0.037}C_{0.346}$ composite. Observed (dots), calculated (line) and difference (below) curves are shown. The vertical marks show the Bragg positions for the $Ni_{3.4}Sn_4$, Si and Sn phases. The scattered bump on the background indicates an amorphous phase.

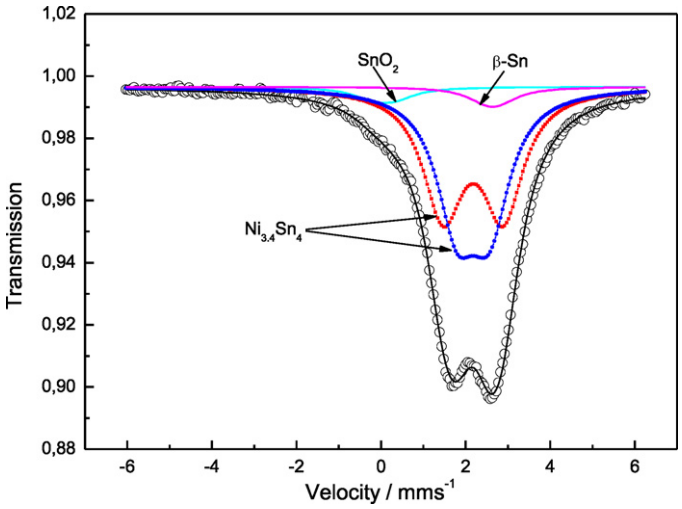

Fig. 4. ^{119}Sn Mössbauer spectrum of $Ni_{0.14}Sn_{0.17}Si_{0.32}Al_{0.037}C_{0.346}$ at room temperature. Experimental data (circles) and the adjusted curve (line) are shown. Three phases are identified: $Ni_{3.4}Sn_4$ (dots and squares doublets), β-Sn and SnO_2.

Fig. 4 shows ^{119}Sn Mössbauer spectrum of the 20 h-milled composite obtained by TMS. It is fitted using two main doublets (dots and squares lines in Fig. 4) centered at 2.09 mm s^{-1} with different quadrupole splittings (0.77 and 1.42 mm s^{-1}) and equal relative intensities [21]. A good fit of the experimental data is only obtained by adding two minor doublets at 2.55 mm s^{-1} and 0.00 mm s^{-1} and attributed respectively to β-Sn and traces of Sn(IV). The hyperfine parameters of the Sn(IV) compound (Table 2) are close to the ones usually obtained for SnO_2 [22]. Relative amounts of Sn-containing phases (Table 2) have been obtained from the relative areas by assuming the Lamb–Mössbauer factors to be respectively 0.2, 0.05 and 0.5 for $Ni_{3.4}Sn_4$, β-Sn and SnO_2 [23–25]. It is worth noting that the Sn(IV) can be explained by either the surface oxidation of the precursor or by accidental oxidation of tin during the preparation process. Because of the low content of Sn(IV) (less than 1%), it will be neglected in the next paragraphs.

By combining the Mössbauer quantification of tin compounds and the XRD results for the crystalline phases, one can suggest a detailed chemical composition for the composite. On one hand Mössbauer analysis evidenced that tin is essentially present as β-Sn and $Ni_{3.4}Sn_4$. The relative amounts of these two phases can be written as:

$$0.03Sn + 0.034Ni_{3.4}Sn_4 \quad (1)$$

To equilibrate Eq. (1), it is necessary to add 0.024 Ni and if we assume that all this nickel is contained in the amorphous by-product "Ni–Si", Eq. (1) can be written as:

$$0.03Sn + 0.034Ni_{3.4}Sn_4 + 0.024\text{“Ni–Si”} \quad (2)$$

Knowing from XRD results that Si constitutes about 83.9 at.% of the crystalline matter corresponding to about 0.27 Si, the rest of 0.05 Si is contained in the by-product. To equilibrate the Si content, the by-product should have about 2 Si for 1Ni and hence has been attributed to nickel silicide "$NiSi_2$". The STEM-EDX shows that Al is randomly distributed in the material and it is not easy to associate it to one of the identified phases. The final composition can thus be given as:

$$0.03\beta\text{-}Sn^{cryst} + 0.034Ni_{3.4}Sn_4{}^{cryst} + 0.27Si^{cryst} + 0.024\text{“}NiSi_2\text{”}^{amorph} + 0.037Al + 0.346C \quad (3)$$

The composition of the amorphous phase as $NiSi_2$ type is only tentative and should be confirmed by further analyses.

Table 1
Microstructural data of the crystalline phases $Ni_{3.4}Sn_4$, Si and β-Sn from Rietveld analysis of 20 h-milled $Ni_{0.14}Sn_{0.17}Si_{0.32}Al_{0.037}C_{0.346}$ composite (Fig. 3). For comparison pure elements Si and Sn and pure phase $Ni_{3.4}Sn_4$ are given. Standard deviations referring to the last significant digits are given in brackets.

Sample	Phases	Unit-cell parameters				Space group	Content (mol.%)	Crystallite size (nm)
		a (Å)	*b* (Å)	*c* (Å)	*β* (°)			
$Ni_{0.14}Sn_{0.17}Si_{0.32}$	$Ni_{3.4}Sn_4$	12.398 (1)	4.063 (3)	5.200 (5)	104.238 (7)	*C*2/*m*	12 (1)	6 (1)
$Al_{0.037}C_{0.346}$	Si	5.430 (3)	–	–	–	*Fd*$\bar{3}$*m*	84 (1)	14 (1)
	β-Sn	5.841 (1)	–	3.183 (7)	–	*I*4$_1$/*amd*	4 (1)	9 (1)
Pure elements	Si	5.426 (3)	–	–	–	Fd$\bar{3}$m	100	>100
	β-Sn	5.829 (1)	–	3.179 (7)	–	*I*4$_1$/*amd*	100	>100
Pure $Ni_{3.4}Sn_4$	$Ni_{3.4}Sn_4$	12.435 (3)	4.078 (3)	5.209 (3)	103.67 (2)	*C*2/*m*	100	>100

Table 2
Hyperfine parameters of ^{119}Sn Mössbauer spectrum shown in Fig. 4: *δ*, isomer shift relative to $BaSnO_3$; *Δ*, quadrupole splitting; and relative area (%).

Phases	Sites	*δ* (mm s^{-1})	*Δ* (mm s^{-1})	Relative areas (%)	Relative amounts (at.%)
$Ni_{3.4}Sn_4$	4i$_1$	2.09	0.77	46	40.5
	4i$_2$	2.09	1.42	46	40.5
β-Sn		2.55	0.29	5	18
SnO_2		0.00	0.52	3	1

SEM images of the 20 h-milled composite morphology are shown in Fig. 5. The composite consists of large agglomerates typically some tens of microns in size (Fig. 5a). The agglomerates are formed by spherical particles with typical size around 150 nm (and varying from 20 to 400 nm) embedded in a shapeless matrix (Fig. 5b and c). Backscattered electron mode detection (Fig. 5d) shows a contrast difference between the particles and the matrix indicating the composition difference. The dark contrast of the matrix is attributed to its large carbon content. Chemical analysis by EDX was not realizable because of the low spatial resolution of the detector comparing to the nanostructured phase composition of the composite.

TEM and HRTEM analysis were carried out for a better characterization of the composite microstructure (Fig. 6). As shown in Fig. 6a, the composite microstructure consists of spherical particles of ~150 nm average size diameter (varying between 30 nm and 220 nm) surrounded by a complex nanostructured matrix. STEM-EDX analysis indicates that the spherical particles are pure Si. A schematic representation of this microstructure is given in Fig. 6b. The matrix contains nanocrystallized domains smaller than 5 nm, as revealed from high resolution TEM (Fig. 6c) and inverse Fast Fourier Transform (FFT) analysis (Fig. 6d). This observation is in good agreement with XRD results which showed the occurrence of major $Ni_{3.4}Sn_4$ phase with average crystallite size about 6 ± 1 nm.

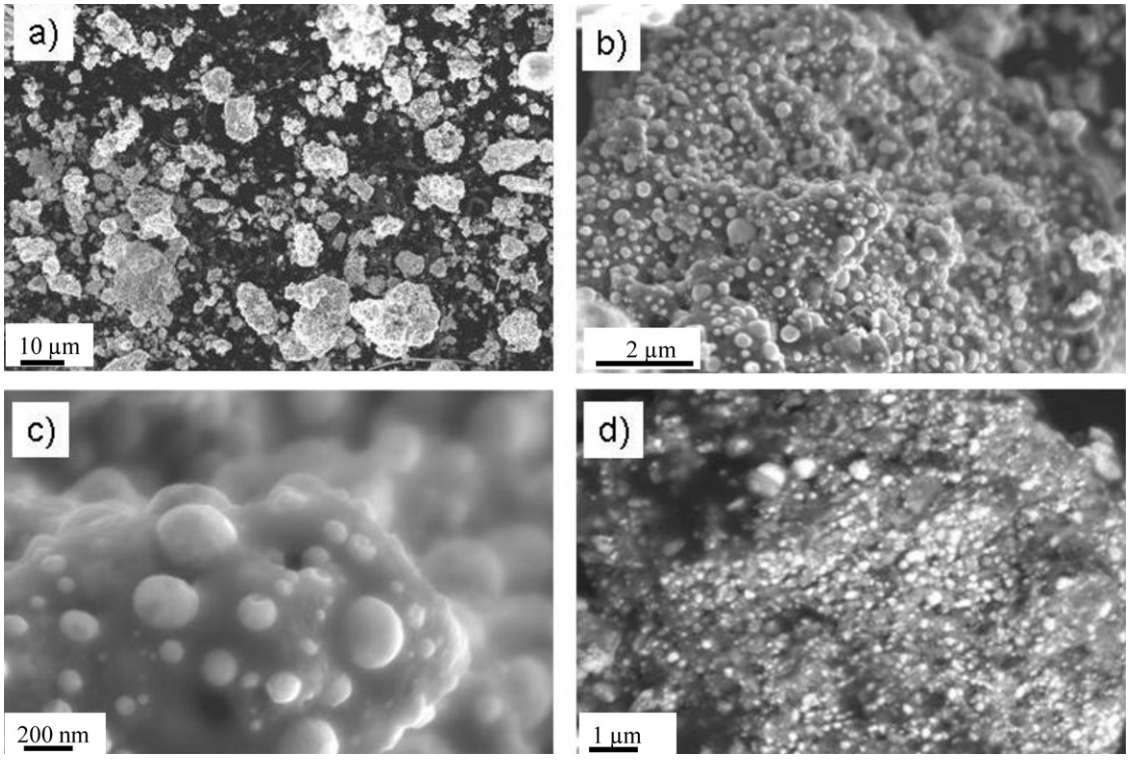

Fig. 5. SEM micrographs showing the morphology of the 20 h-milled $Ni_{0.14}Sn_{0.17}Si_{0.32}Al_{0.037}C_{0.346}$ composite. (a, b and c) Secondary electron images with in-lens detector at different magnifications. (d) Backscattered electron image.

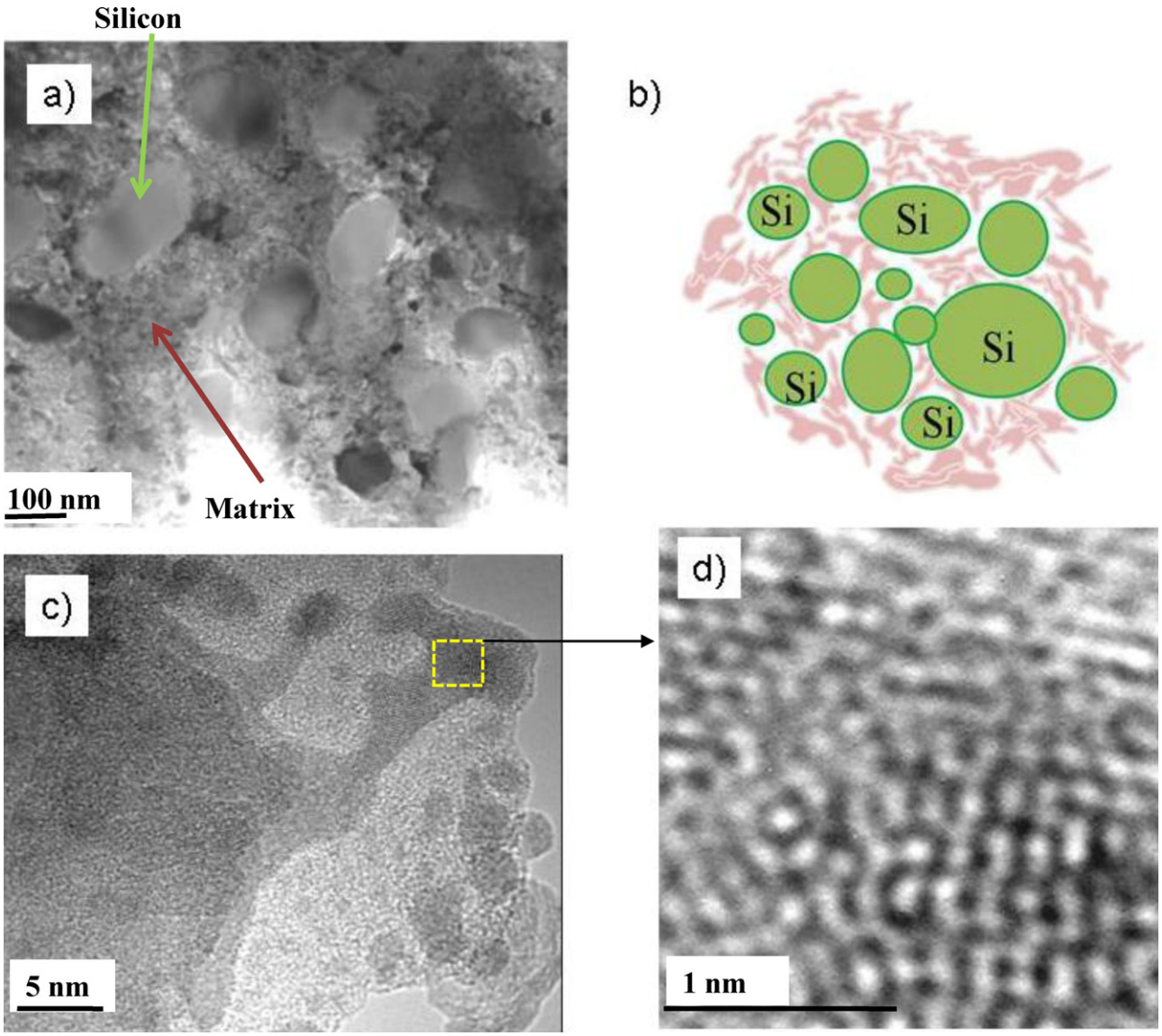

Fig. 6. TEM images of the 20 h-milled $Ni_{0.14}Sn_{0.17}Si_{0.32}Al_{0.037}C_{0.346}$ composite. (a) Bright field image showing the overall composite microstructure, (b) schematic representation of the composite microstructure, (c) magnification of the matrix microstructure in bright field mode, and (d) inverse FFT analysis of the matrix showing its nanocrystallinity.

Chemical analysis of the matrix has been performed in STEM-EDX mode and the results are shown in Fig. 7. The chemical composition of the matrix is complex. It contains Sn, Ni, Si and Al elements though not equally distributed. Ni and Sn signals are spatially correlated in agreement with the occurrence of the $Ni_{3.4}Sn_4$ phase as proved by XRD and TMS. The Si signal is anticorrelated to the previous ones showing low solubility of Si in the $Ni_{3.4}Sn_4$ phase. Finally, Al is evenly distributed over the whole matrix. Unfortunately, we could not analyze the C distribution in the matrix due to the beam contamination which adds a significant quantity of carbon leading to inaccurate results. Nonetheless it is expected to be distributed around Si and $Ni_{3.4}Sn_4$ phases occupying a significant volume of the matrix.

3.2. Electrochemical characterization

The 20 h-milled $Ni_{0.14}Sn_{0.17}Si_{0.32}Al_{0.037}C_{0.346}$ composite has been studied electrochemically in a half-coin type cell. Fig. 8 shows the profiles of the first three galvanostatic cycles realized at a rate of *C*/50. The first cycle was carried out between the rest potential Ei (V) and 0 V (vs. Li^+/Li^0), the second was between 2 V and 10 mV and the third one between 2 V and 70 mV. Choices of the cut-off potentials for the three first cycles were done respectively with the aim of activating Si particles, to obtain the maximal capacity avoiding lithium deposition on the active material and to increase battery cycle-life. Remember that here the term charge is used for lithiation and discharge for delithiation. At the first charge, during lithiation, a capacity of 1586 mAh g^{-1} is achieved. The first charge profile exhibits two distinct features. Firstly a rapid potential drop is noted between Ei (V) and 0.5 V with a kink at 1.3 V that indicates the beginning of the formation of the solid–electrolyte interface (SEI) [8]. This region is irreversible as it appears only at the first charge. The second feature is a large sloping plateau between 0.5 and 0 V. This plateau can be a result of a combination of both Si and $Ni_{3.4}Sn_4$ lithiations. Indeed it is well known that nanosized Si forms Li–Si alloys at low potentials majorly $Li_{12}Si_7$ alloy at 0.1 V at room temperature [26]. Furthermore, Ni_3Sn_4 lithiation was investigated by several groups [8–10,20,21]. The study of the first electrochemical cycle profile for Ni_3Sn_4 shows two stages during lithiation: a gradual potential decrease from 0.5 V to 0.1 V followed by a large

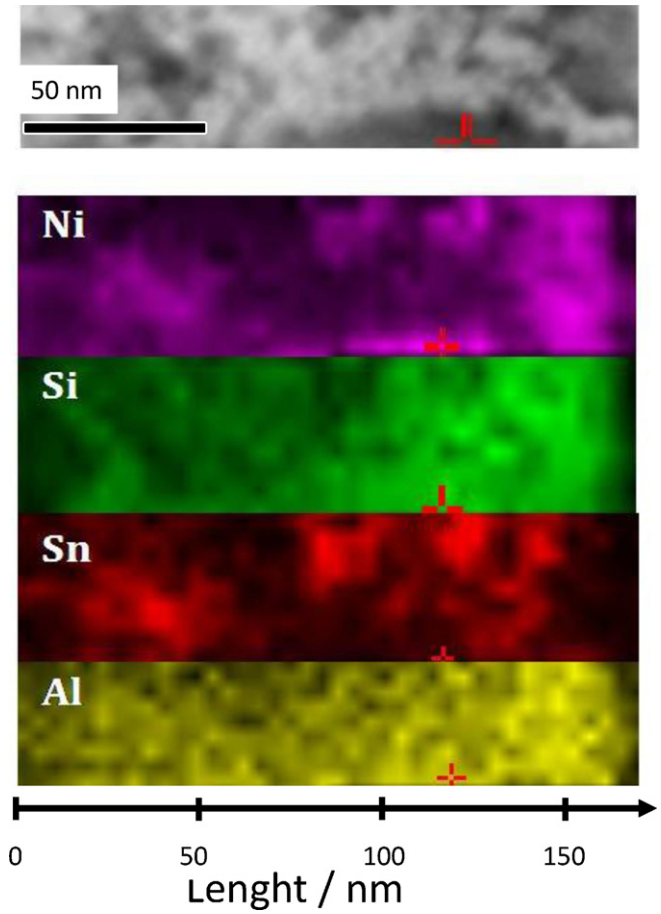

Fig. 7. Drift corrected STEM image (top) and EDX chemical mapping of Ni, Si, Sn and Al elements in the matrix region of the 20 h-milled $Ni_{0.14}Sn_{0.17}Si_{0.32}Al_{0.037}C_{0.346}$ composite.

plateau very close to 0 V. It has been proved by different characterization techniques that the first stage is due to the surface oxide SnO reduction (a thin layer of SnO on the surface consuming Li) whereas the large plateau results from Li_7Sn_2 alloy formation [8]. It is important to note the absence of Li–Sn plateaus in our results (Fig. 8), which indicates the reversibility of Ni_3Sn_4 reaction with Li and thus the absence of metallic tin liberation after the first delithiation. In another study [10], it was found that Li reacts with Sn atoms at and within the grain boundaries of Ni_3Sn_4. Sn atoms are then active but not aggregating into large regions. This is in good agreement with the results presented above. In our case all of these phenomena are assembled in a very close potential region resulting on a smooth slope. Upon discharge a capacity of 1259 mAh g^{-1} is restored corresponding to delithiation reactions. The irreversible capacity at the first cycle is as high as 20.6% corresponding to the SEI layer formation. The high irreversible capacity can be associated to the large surface area for this composite (BET surface equal to 3.5 m^2 g^{-1}). The second and third cycle profiles are both similar and smooth. The same sloping plateaus at lower potentials are noted due to the reversible lithiation reactions of $Ni_{3.4}Sn_4$ and Si with Li.

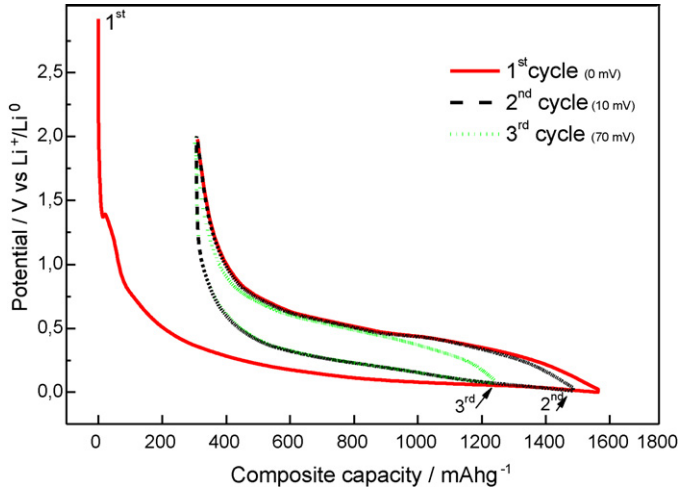

Fig. 8. Galvanostatic charge–discharge lithiation profiles of the 20 h-milled $Ni_{0.14}Sn_{0.17}Si_{0.32}Al_{0.037}C_{0.346}$ composite at *C*/50. The voltage at the end of lithiation is indicated between brackets.

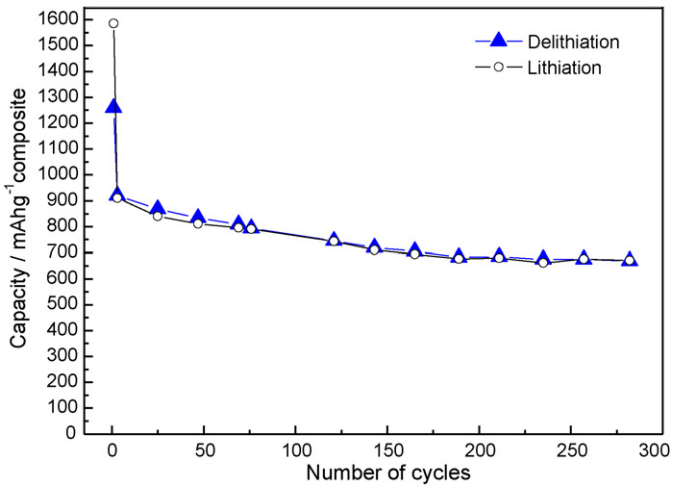

Fig. 9. Charge and discharge capacities vs. cycle number of the 20 h-milled $Ni_{0.14}Sn_{0.17}Si_{0.32}Al_{0.037}C_{0.346}$ composite at *C*/50.

Fig. 9 displays both charge and discharge capacities versus cycle number for the potential range from 70 mV to 2 V. Coulombic efficiency is close 100% except for the first cycle. The reversible capacity obtained by this composite reaches 920 mAh g^{-1} at the third cycle. Upon cycling an average decrease of 0.1% of the capacity per cycle is noted up to 280 cycles. Such an excellent behavior is attributed to the presence of carbon and the nanostructured $Ni_{3.4}Sn_4$ phase which not only buffer volume changes of Si but also shows very interesting capacity retention upon cycling.

4. Conclusion

A nanostructured $Ni_{0.14}Sn_{0.17}Si_{0.32}Al_{0.037}C_{0.346}$ composite has been synthesized by mechanical milling of elemental Si, Al and C graphite powders and $Ni_{3.4}Sn_4$ intermetallic precursor. XRD, SEM, TEM and TMS analyses show that the composite microstructure consists of Si particles with an average particle-size close to 150 nm embedded in a nanostructured and multi-element matrix. This matrix contains 6 nm in size $Ni_{3.4}Sn_4$ precipitates and disordered carbon as major phases with minor amounts of β-Sn and amorphous Si–Ni phases.

This composite is a very promising anode material for Li-ion batteries since it shows a high reversible capacity reaching 920 mAh g^{-1} with a good stability for 280 cycles. The capacity is provided by lithiation of both Si and $Ni_{3.4}Sn_4$ phases, whereas the good stability is attributed to buffering of electrode volume variations by Ni and C elements.

For practical applications, reaction kinetics, cathode compatibility, optimization of electrode composition and shape have to be considered. Research on these topics is underway.

Acknowledgements

Special thanks to the help of Dr. E. Leroy for realizing the TEM imaging and chemical analysis and V. Lalanne for preparing the TEM samples.

References

[1] T.B. Reddy, S. Hossain, Handbook of Batteries (2002) 34.1–34.62 (Chapter 34).
[2] G.M. Ehrlich, Handbook of Batteries (2002) (Chapter 34).
[3] R. Yazami, Electrochim. Acta 45 (1999) 87–97.
[4] A.N. Dey, J. Electrochem. Soc. 118 (1971) 1547.
[5] L.Y. Beaulieu, K.C. Hewitt, R.L. Turner, A. Bonakdarpour, A.A. Abdo, L. Christensen, K.W. Eberman, L.J. Krause, J.R. Dahn, J. Electrochem. Soc. 150 (2003) A149–A156.
[6] U. Kasavajjula, C. Wang, A.J. Appleby, J. Power Sources 163 (2007) 1003–1039.
[7] J. Wolfenstine, J. Power Sources 79 (1999) 111–113.
[8] K.K.D. Ehinon, S. Naille, R. Dedryvère, P.-E. Lippens, J.-C. Jumas, D. Gonbeau, Chem. Mater. 20 (2008) 5388–5398.
[9] X.Q. Cheng, P.F. Shi, J. Alloys Compd. 391 (2004) 241–244.
[10] H.Y. Lee, S.W. Jang, S.M. Lee, S.J. Lee, H.K. Baik, J. Power Sources 112 (2002) 8–12.
[11] S. Naille, R. Dedryvère, D. Zitoun, P.E. Lippens, J. Power Sources 189 (2009) 806–808.
[12] S. Naille, R. Dedryvère, H. Martinez, S. Leroy, P.E. Lippens, J.-C. Jumas, D. Gonbeaub, J. Power Sources 174 (2007) 1086–1090.
[13] C.Q. Zhang, J.P. Tu, X.H. Huang, Y.F. Yuan, S.F. Wang, F. Mao, J. Alloys Compd. 457 (2008) 81–85.
[14] M.S. Park, Y.M. Kang, S. Rajendran, H.S. Kwon, J.Y. Lee, Mater. Chem. Phys. 100 (2006) 496–502.
[15] G.X. Wang, L. Sun, D.H. Bradhurst, S. Zhong, S.X. Dou, H.K. Liu, J. Power Sources 88 (2000) 278–281.
[16] A.H. Whitehead, J.M. Elliott, J.R. Owen, J. Power Sources 81–82 (1999) 33–38.
[17] Z. Wang, W.H. Tian, X.H. Liu, Y. Li, X.G. Li, Mater. Chem. Phys. 100 (2006) 92–97.
[18] T.D. Hatchard, J.M. Topple, M.D. Fleischauer, J.R. Dahn, Electrochem. Solid-State Lett. 6 (2003) A129–A132.
[19] J. Rodríguez-Carvajal, Physica B 192 (1993) 55–69.
[20] S. Furuseth, H. Fjellvag, Acta Chem. Scand. A 40 (1986) 695–700.
[21] S. Naille, P.E. Lippens, F. Morato, J. Olivier-Fourcade, Hyperfine Interact. 167 (2006) 785–790.
[22] C. Nayral, E. Viala, P. Fau, F. Senocq, J.C. Jumas, A. Maisonnat, B. Chaudret, Chem.-Eur. J. 6 (2000) 4082–4090.
[23] C. Hohenemser, Phys. Rev. 139 (1965) A185–196.
[24] M.T. Sougrati, S. Jouen, B. Hannoyer, Hyperfine Interact. 167 (2006) 815–818.
[25] R.C. Reno, M.J. Panunto, B.H. Piekarski, J. Electron. Mater. 26 (1997) 11–15.
[26] B. Gao, S. Sinha, L. Fleming, O. Zhou, Adv. Mater. 13 (2001) 816–819.